Journal of Solid State Chemistry 183 (2010) 3029–3038

Contents lists available at ScienceDirect

Journal of Solid State Chemistry

journal homepage: www.elsevier.com/locate/jssc

In situ X-ray absorption spectroscopic investigation of the electrochemical conversion reactions of CuF_2–MoO_3 nanocomposite

A.N. Mansour [a,*], F. Badway [b], W.-S. Yoon [c], K.Y. Chung [d], G.G. Amatucci [b]

[a] Systems and Materials for Power and Protection Branch, Naval Surface Warfare Center, Carderock Division, 9500 MacArthur Boulevard, West Bethesda, MD 20817-5700, USA
[b] Energy Storage Research Group, Department of Materials Science and Engineering, Rutgers, The State University of New Jersey, North Brunswick, NJ 08902, USA
[c] School of Advanced Materials Eng., Kookmin University, 861-1 Jeongneung-dong, Seongbuk-gu, Seoul 136-702, Republic of Korea
[d] Battery Research Center, Korea Institute of Science and Technology, Seoul 136-791, Republic of Korea

ARTICLE INFO

Article history:
Received 26 May 2010
Received in revised form
14 September 2010
Accepted 22 September 2010
Available online 8 October 2010

Keywords:
Copper fluorides
Conversion reactions
Energy storage
X-ray absorption spectroscopy
Redox couple
Lithium batteries
Nanocomposite

ABSTRACT

We have used X-ray absorption spectroscopy at the Cu *K*-edge to investigate the electrochemical conversion reaction of 20 nm size 85 wt% CuF_2 – 15 wt% MoO_3 nanocomposite under in situ conditions. The nanocomposite was prepared by high energy milling. Upon discharge, the lithiation reaction with the nanocomposite resulted in the formation of nanophase metallic Cu, which is consistent with the conversion of CuF_2 into Cu and LiF. Based on XANES and Fourier transforms of EXAFS spectra, we show that the discharge process proceeded via the formation of highly dispersed Cu particles. Based on the coordination number of the first shell of Cu, the average size of the Cu particles was estimated to be in the 1–3 nm range in the fully discharged state.

1. Introduction

Metal fluorides have gained some renewed interest lately for their theoretical high energy density [1,2]. The recently introduced metal fluoride nanocomposites using carbon or metal dichalcogenide matrices has enabled the electrochemical activity of the class of high voltage, high energy density metal fluorides [3–8]. In contrast to the ubiquitous intercalation reaction of present day metal oxides positive electrode materials, the reversible conversion mechanism by which some of these metal fluorides operate resulted in demonstrated specific capacities in excess of 600 mAh/g and energy densities of 1300 Wh/kg. Although cycle life is limited to <100 cycles for most materials at this early stage, these materials offer an interesting path forward for next generation positive electrode materials.

Of all the transition metal fluorides that could be enabled one of the attractive materials is CuF_2. CuF_2 has a theoretical conversion potential of 3.55 V based on thermodynamic calculations [9]. Combined with a theoretical discharge specific capacity of 528 Ah/kg leads to an exceptionally high energy density of 1874 Wh/kg. Indeed such values are almost 300% higher than those attained for the positive electrode of present day state of the art rechargeable Li batteries based on the $LiCoO_2$ intercalation compound. With respect to existing primary cathode compounds, CuF_2 would exceed the widely utilized MnO_2 specific energy by almost a factor of 2. In addition, the CuF_2 volumetric energy density (7870 Wh/L) would exceed the volumetric energy density of carbon monofluoride (approx. 6000 Wh/L) with a possible advantage of faster discharge rates.

CuF_2 was studied for its application as a potential high energy density electrode a number of decades ago [10–14]. However, full utilization of a nonhydrated material was never reported and the material lost favor. Recently, the full theoretical specific capacity of the material was achieved using the mixed conductive nanocomposites [15]. In this case, a small amount of mixed conducting $MoO_{3-x}F_x$ was formed in situ by a high energy milling of MoO_3 and CuF_2. This paper is an in depth analysis of the lithiation reaction of such nanocomposites by X-ray absorption spectroscopy (XAS) under in situ conditions.

2. Experiment

2.1. Nanocomposite fabrication

Nanocomposites were fabricated by the introduction of approximately 1 g of copper fluoride (CuF_2) into a high-energy milling cell along with 15 wt% MoO_3 conductive matrix. The as-received CuF_2 (Aldrich) was anhydrous and was verified using

* Corresponding author.
E-mail address: Azzam.Mansour@navy.mil (A.N. Mansour).

0022-4596/$ - see front matter © 2010 Elsevier Inc. All rights reserved.
doi:10.1016/j.jssc.2010.09.029

XRD and FTIR. The cell was sealed under helium and high energy milled (HEM) for various times in a Spex 8000 milling apparatus. Afterwards, the cell was opened and the contents were removed in the helium atmosphere of the glove box. Based on an XAS investigation of the nanocomposite at the Cu and Mo *K*-edges [15], the oxidation states of Cu and Mo in the nanocomposite were reduced relative to the nominal values of CuF_2 and MoO_3. The slight reduction in the oxidation states of Cu and Mo combined with XRD results was consistent with anion exchange between CuF_2 and MoO_3. Based on the XAS and XRD results, the nanocomposite was found to consist of $CuF_{1.9}O_{0.02}$ and $MoO_{2.2}F_{0.8}$. For simplicity, hereafter, the nanocomposite is referred to frequently as CuF_2–MoO_3.

2.2. Electrode fabrication and discharge conditions

Electrodes were prepared by adding poly(vinylidene fluoride-co-hexafluoropropylene) (Kynar 2801, Elf Atochem), carbon black (Super P, MMM) and dibutyl phthalate (DBP) (Aldrich) to the active materials in acetone. The slurry was tape cast onto a 10-μm-thick Al foil, dried for 1 h at 22 °C, and rinsed in 99.8% anhydrous ether (Aldrich) to extract the DBP plasticizer. The electrodes, 3.14 cm^2 disks typically containing $57 \pm 1\%$ active material and $13 \pm 1\%$ carbon and 30% Kynar 2801, were tested electrochemically versus Li metal (Johnson Matthey). The estimated theoretical capacity of the nanocomposite electrode analyzed by in situ XAS was 11.0 mAh based on a nanocomposite (85 wt% CuF_2–15 wt% MoO_3) loading of 7.8 mg/cm^2 and a theoretical capacity of 528 mAh/g of CuF_2. The electrodes were assembled into a specially designed spectroelectrochemical cell [16] in an argon-filled dry box using Celgard separators saturated with 1 M of $LiPF_6$ in an ethylene carbonate (EC) and dimethyl carbonate (DMC) electrolyte (Merck) with EC:DMC volume ratio of 1:1. The cell was discharged to 2.0 V and recharged to 4.2 V vs. Li/Li^+ at 24 °C using a constant current of 0.4 mA, which corresponds to 19.2 mA/g of CuF_2. The open circuit voltage of the fresh cell was measured to be 3.58 V vs. Li/Li^+.

2.3. X-ray absorption spectroscopy (XAS) experiments

The XAS experiments were conducted on the bending magnet station X-11 A of the National Synchrotron Light Source with the electron storage ring operating at electron energy of 2.8 GeV and a stored current in the range 200–300 mA [17]. The X-ray absorption fine structure (XAFS) spectra were collected in the transmission mode at room temperature with a variable exit double-crystal monochromator using two flat Si(111) crystals. The energy resolution at the Cu *K*-edge was estimated to be 2.5 eV compared to the core hole line width of 1.55 eV [18]. The harmonic-content of the beam was minimized by controlling the parallelism of the monochromator crystals to reduce the beam intensity by 20%. The incident and transmitted X-ray intensities were monitored using ionization chambers (30 cm long) with appropriate mixtures of nitrogen and argon flowing through the chambers, which were adjusted to yield about 25% and 60% absorption for the incident and transmitted X-rays, respectively. The energy calibration of the monochromator was monitored using a 5-μm-thick Cu foil placed between the transmitted beam chamber and a third ionization chamber (15 cm long) having the same fill gas as the transmitted beam chamber. The X-ray absorption edge jump for the electrode was ~1.2 which is below 1.5 in order to minimize the effects of pinholes and particle size on XAFS amplitudes [19,20].

2.4. X-ray absorption spectroscopy data analysis

The X-ray absorption spectra were calibrated with respect to the first inflection point energy of the *K*-edge of a Cu foil at 8979 eV. The *K*-edge absorption was isolated by fitting the pre-edge region (−300 to −30 eV) with the Victoreen formula, extrapolating over the entire range of the spectrum, and subtracting the background from the entire spectrum. Energy independent step normalization was applied by dividing the absorption cross section with the value of the average absorption in the range 100–400 eV above the edge energy. The extended X-ray absorption fine structure (EXAFS), $\chi(k)$, was extracted using multi-node cubic spline procedures, which minimized the amplitude of non-physical peaks in the 0–0.9 Å region of the Fourier transform [21,22]. The data analysis up to this point was carried out using the WinXAS software package (version 3.1) [23,24].

All fits were made using the curve fitting code FEFFIT of the UWXAFS software package [25]. The data were fitted using theoretical standards calculated based on the curved-wave scattering formalism of the FEFF Code (version 8.2) [26,27]. The FEFF calculations were performed using established structural models for Cu [28] and CuF_2 [29,30]. The Fourier transforms were generated using k^3-weighted EXAFS spectra over the range 3.0–12.8 $Å^{-1}$ with a Hanning window of 1.0 $Å^{-1}$. The fits for the CuF_2–MoO_3 nanocomposite were performed in real space over the range 0.85–3.9 Å. In fitting the data, the many body amplitude reduction factor (S_0^2) was floated while the coordination numbers (N) of various shells were constrained to their crystallographic values. The coordination distances (R) and disorders (σ^2) of various shells were floated under the following constraints: (1) the two Cu–F equatorial distances were constrained to differ from the crystallographic values by the same amount, (2) the apical and more distant Cu–F distances were constrained to differ from the crystallographic values by the same amount, (3) the Cu–Cu distances were constrained to differ from the crystallographic values by the same amount, (4) the disorders for the two Cu–F equatorial distances were assumed to be similar, (5) the disorders for the apical and more distant Cu–F contributions were assumed to be similar, and (6) the disorders for the Cu–Cu contributions were assumed to be similar. One inner potential (E_0) was used in the analysis of the multiple shell fits and a Gaussian disorder was assumed for all shells. The number of fitting parameters was kept below the maximum number of independent data points allowed by the Brillouin theorem [31]. The number of degrees of freedom is given as the difference between the number of independent data points and the number of floating parameters. The goodness of each fit is given by the value of the *R*-factor, which is the sum of the square of residuals between measured and model data normalized to the magnitude of the measured data.

3. Results and discussion

3.1. The structure of CuF_2

The structure of CuF_2 was first determined by Fischer et al. [29] and later refined by Burns and Hawthorne [30]. In both studies, the crystal structure was adequately described as a monoclinic lattice with space group as $P2_1/c$ or $P2_1/n$. A schematic of the structure of CuF_2 is shown in Fig. 1. The local structure parameters of CuF_2 as determined from the refined X-ray diffraction data of Burns and Hawthorne [30] are listed in Table 1. The local structure of Cu consists of a highly distorted octahedron (CuF_6) due to the Jahn–Teller distortion. The equatorial Cu–F distances are slightly distorted but the apical Cu–F distance is significantly larger than

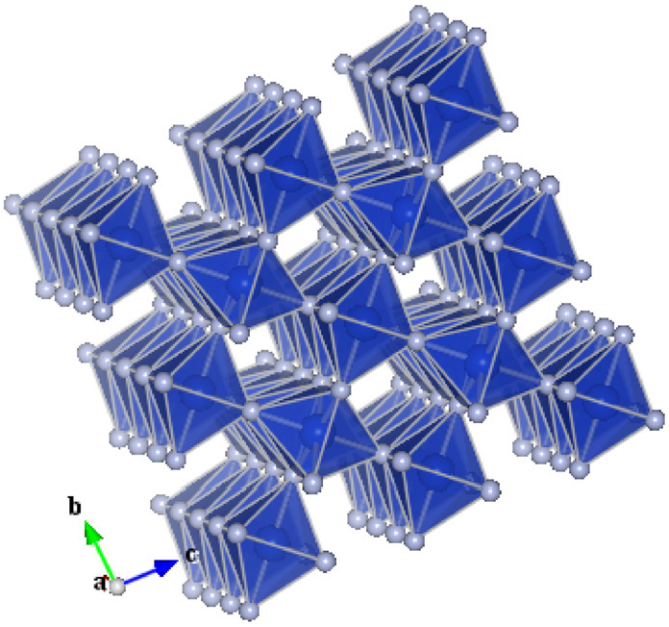

Fig. 1. The structure of CuF_2 displaying the highly distorted octahedral coordination of Cu and the 1×1 tunnel structure.

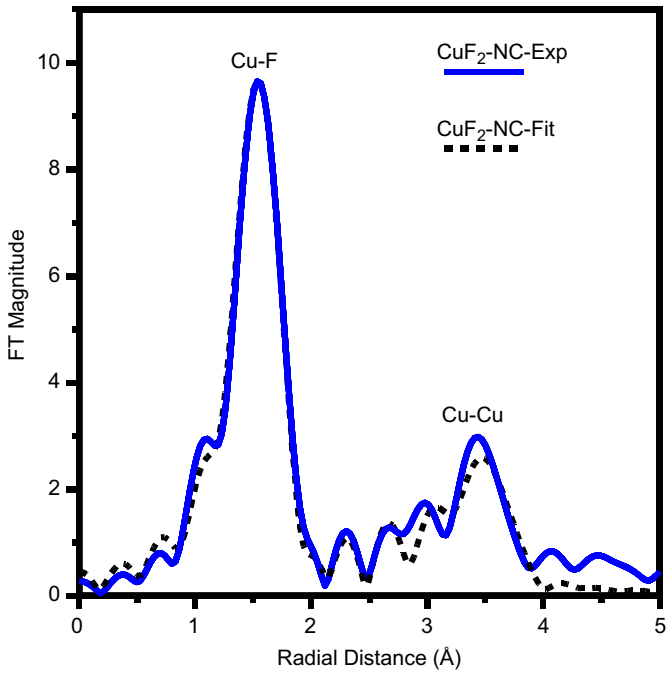

Fig. 2. Comparison of the experimental and simulated Fourier transforms (FT) of k^3-weighted Cu *K*-edge EXAFS spectra for the 85 wt% CuF_2–15 wt% MoO_3 nanocomposite. The local structure parameters used for the simulated Fourier transform are listed in Table 1. The FT window is 3.0–12.8 $Å^{-1}$.

Table 1
Summary of local structure parameters (*N* and *R*) based on the refined X-ray diffraction data for CuF_2 (Ref. [30]). We also included a summary of local structure parameters based on quantitative analysis of Fourier transforms of k^3-weighted EXAFS spectra for the 85 wt% CuF_2–15 wt% MoO_3 nanocomposite. The Fourier transforms of k^3-weighted EXAFS spectra over the range 3–12.8 $Å^{-1}$ were refined in the 0.85–3.9 Å region.

CuF_2 (XRD)[a]			CuF_2 nanocomposite (EXAFS)[b]	
X–*Y*pair	*N*	*R* (Å)	*R* (Å)[c]	$\sigma^2(10^{-3}Å^2)$[c]
Cu–F	2	1.902	1.904 (5)	4.3 (7)
Cu–F	2	1.932	1.934 (5)	4.3 (7)
Cu–F	2	2.318	2.302 (26)	16.7 (41)
Cu–Cu	2	3.297	3.317 (8)	8.6 (7)
Cu–F	2	3.491	3.476 (26)	16.7 (41)
Cu–Cu	4	3.516	3.535 (8)	8.6 (7)
Cu–F	2	3.541	3.525 (26)	16.7 (41)
Cu–Cu	4	3.760	3.780 (8)	8.6 (7)

[a] Results based on the refined XRD data (Ref. [30]) for the FEFF calculations.
[b] The many body amplitude reduction factor (S_0^2) and the inner potential (E_0) were determined to be 0.85 (8) and 0.1 (1.3) eV, respectively. The *R*-factor for this fit is 0.0177.
[c] Uncertainties in the last digit(s) are given in parentheses.

the equatorial distances. The extent of the octahedron distortion is slightly higher in the refined XRD study reported by Burns and Hawthorne [30].

3.2. XAFS results for the 85 wt% CuF_2–15 wt% MoO_3 nanocomposite cathode:

The Fourier transform of the k^3-weighted Cu *K*-edge extended-XAFS (EXAFS) spectrum generated over the range 3.0–12.8 $Å^{-1}$ for the nanocomposite cathode is shown in Fig. 2. It is to be noted that distances in the Fourier transform are lower by about 0.2–0.3 Å relative to the crystallographic values due to the phase shifts introduced by the central absorbing and backscattering atoms. This shift is taken into account during the quantitative analysis of EXAFS spectra and Fourier transforms. Furthermore, coordination spheres with distance separation $\delta R < \pi/2k_{max}$ cannot be resolved in the Fourier transforms. In this case, $\delta R = 0.12$ Å for a k_{max} of 12.8 $Å^{-1}$. Interferences from closely spaced coordination spheres can produce features or peaks in the Fourier transform that do not correspond to the true crystallographic distances.

The Fourier transform displays a strong peak, which corresponds to the first shell of CuF_6 octahedron. The moderate intensities beyond the first shell correspond to several contributions from distant shells dominated by scattering from the Cu atoms (see Table 1 for details). The 0.85–3.9 Å region of the Fourier transform was refined using the backscattering amplitudes and phases derived from the refined XRD structural model, which is described in Table 1. The refinement of the Fourier transform was performed using the procedure described in the XAFS data analysis subsection. The Fourier transform generated based on the refined XRD model is also displayed in Fig. 2 showing good agreement with the experimental data. By constraining the coordination numbers to their crystallographic values, the many body amplitude reduction factor (S_0^2) is estimated to be 0.85 ± 0.08, which is consistent with that previously reported for CuF_2 and some nanocomposites [15]. The equatorial Cu–F distances are close to those reported based on the refined XRD study. The Cu–Cu distances are about 0.02 Å greater than those based on the XRD data. The disorders for the Cu–F equatorial distances are typical of a low degree of disorder. However, the disorders for the Cu–-F apical distance and more distant Cu–F contributions are typical of a high degree of disorder. The disorders for the Cu–Cu distances are slightly larger than that observed for the first shell of metallic Cu (see Table 2 for details).

3.3. XAFS results for the discharged CuF_2–MoO_3 nanocomposite cathode

Unfortunately, the discharge curve which was collected simultaneously with the XAFS measurements was lost and in

Table 2
Summary of local structure parameters based on quantitative analysis of Fourier transforms of EXAFS spectra for the Cu nanoparticles generated as the discharged product of the 85 wt% CuF_2–15 wt% MoO_3 nanocomposite (Cu-NC) and Cu Foil (Cu-FL).

Sample	*X*–*Y* pair	S_0^2	*N*	*R* (Å)	σ^2 (10^{-3} Å^2)	E_0 (eV)	*R*-Factor
Cu FL (EXAFS)	Cu–Cu	0.98(9)	12	2.552(5)	8.9(6)	3.5(11)	0.008
Cu FL (EXAFS)	Cu–Cu	0.85[a]	12	2.550(6)	8.0(2)	3.3(13)	0.011
Cu NC (EXAFS)	Cu–Cu	0.85[a]	9.3(13)	2.535(8)	9.8(9)	3.6(16)	0.016
Cu (XRD)	Cu–Cu		12	2.556			

[a] The many body amplitude reduction factor was constrained to that derived from fitting the FT data for the 85 wt% CuF_2–15 wt% MoO_3 nanocomposite, which yielded a disorder in agreement with well established values for the first shell of metallic Cu.

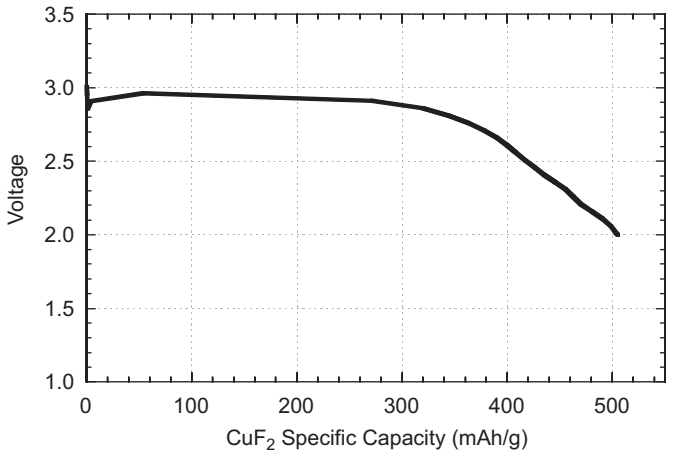

Fig. 3. A typical discharge curve for the CuF_2–MoO_3 nanocomposite discharged at 7.58 mA/g in 1M $LiPF_6$ EC:DMC at 24 °C. The discharge curve which was collected simultaneously with the XAFS data was lost and a substitute curve is included here.

Fig. 3 we included a typical discharge curve for the nanocomposite, which is quite similar but not identical to the original curve. The Cu *K*-edge XANES spectra for the CuF_2 nanocomposite cathode collected during the discharge cycle are shown in Fig. 4 as a function of state of discharge. We also included the reference spectrum for metallic Cu for comparison purposes. The derivatives of these spectra are shown in Fig. 5. The discharge state is given in terms of the specific columbic charge (in mAh/g of CuF_2), assuming that all of the charge was consumed in reducing CuF_2. That is, the charge consumed due to electrolyte decomposition and other possible side reactions (if any) was ignored.

The spectrum, which corresponds to 0 mA, was collected while holding the cell at open circuit voltage (OCV). Based on the dipole selection rules, the peak labeled *B* in the XANES spectrum of CuF_2–MoO_3 nanocomposite (at about 8995 eV) corresponds to the transition from the 1*s* core states to 4*p* states above the continuum threshold in a $3d^9$ electronic configuration [32]. This feature, which appears with a shoulder on the low energy side in the XANES spectra, displays two prominent contributions (B_1 and B_2) when the first derivative of XANES spectra is displayed as shown in Fig. 5. These two contributions correspond to the transitions from the 1*s* core states to the $4p_z$ and $4p_{x,y}$ components of the unoccupied density of states as has been demonstrated based on polarization-dependent XAS investigation [33]. The peak labeled *A* in the XANES spectrum of metallic Cu corresponds to the transition from the 1*s* states to 4*p* states above the continuum threshold in a $3d^{10}$ electronic configuration. A pre-edge peak is also present in the case of the CuF_2 nanocomposite but with extremely weak intensity due to the highly ionic nature of the Cu–F bond. This peak is more evident in the first derivative spectrum of the CuF_2 nanocomposite near 8979 eV as displayed in Fig. 5.

As one discharges the cathode, the intensity of feature *A* in the XANES spectra slowly increases with increase in the state of discharge of the cathode. This feature evolves into a major peak whose position and intensity for the fully discharged cathode closely resemble that of metallic Cu. The increase in the intensity of feature *A* is concomitant with a decrease in the intensity of feature *B* near 8995 eV. Essentially, the XANES spectrum for the fully discharged cathode more closely resembles the XANES spectrum for metallic Cu. Based on the above observations, the discharge mechanism of the CuF_2–MoO_3 nanocomposite cathode can be described by the following reaction: $CuF_2 + 2Li \rightarrow Cu + 2LiF$.

The formation of Cu can be further supported by the EXAFS spectra and Fourier transforms of k^3-weighted EXAFS spectra presented in Figs. 6 and 7, respectively. Initially, the Fourier transforms are dominated by a major peak in the 1–2 Å range, which corresponds to contributions from the distorted coordination of the CuF_6 octahedron and a multi-peak structure in the 3–4 Å range, which is dominated by three distant Cu–Cu contributions from the CuF_2 nanocomposite cathode. Upon discharging the cathode, a unique peak evolves in the 2–3 Å region whose intensity increases with increase in the state of discharge of the nanocomposite cathode. This peak position differs from any of the peak positions observed for the pristine CuF_2 nanocomposite but is similar to that observed for the first shell of metallic Cu as shown in Fig. 7 (bottom set of curves). The formation of metallic Cu and LiF was also confirmed by XRD analysis of a CuF_2–MoO_3 nanocomposite cathode discharged to 75% depth of discharge, as shown in Fig. 8. The direct conversion of CuF_2 into Cu and LiF during the discharge of the CuF_2-MoO_3 nanocomposite is consistent with that reported by Yamakawa et al. [34] for a carbon coated nano-CuF_2 cathode based on a combined X-ray diffraction and NMR investigation. The formation of metallic Cu was also reported during the discharge of xerogel $Cu_{0.1}V_2O_2$ cathodes in lithium cells [35,36]. The conversion reaction was also reported in the case of BiF_3-carbon nanocomposite upon cycling in lithium cells [7]. In this study, the formation of metallic Bi and LiF was confirmed based on Bi L_3 edge XANES and Fourier transforms of EXAFS spectra, X-ray diffraction, and selected area electron diffraction analyses.

The Fourier transforms for the fully discharged CuF_2–MoO_3 nanocomposite cathode and metallic Cu, over the 0–6.0 Å range, are shown in Fig. 9. The Fourier transform for the CuF_2 nanocomposite was also plotted after scaling vertically by a factor of 1.68 in order to scale its first shell amplitude to that of metallic Cu. The Fourier transforms for metallic Cu as well as that of the fully discharged CuF_2–MoO_3 nanocomposite display four major peaks, which correspond to the first, second, third, and fourth shells of Cu–Cu interactions. However, the amplitudes of these peaks are significantly lower in the case of the fully discharged CuF_2–MoO_3 nanocomposite. Even, when the amplitude of the first shell for the fully discharged cathode is rescaled

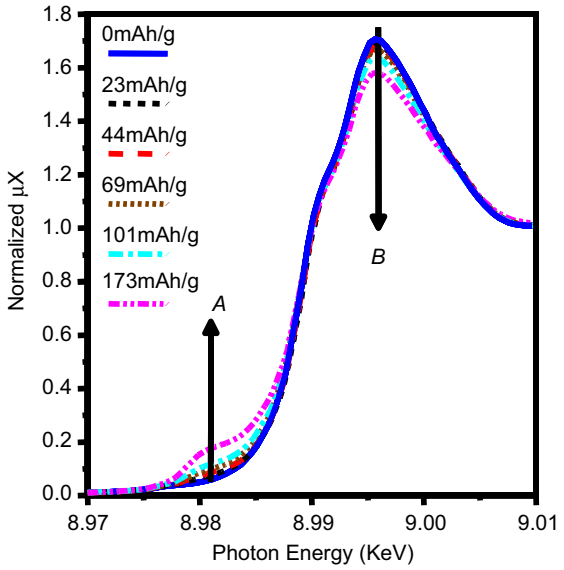

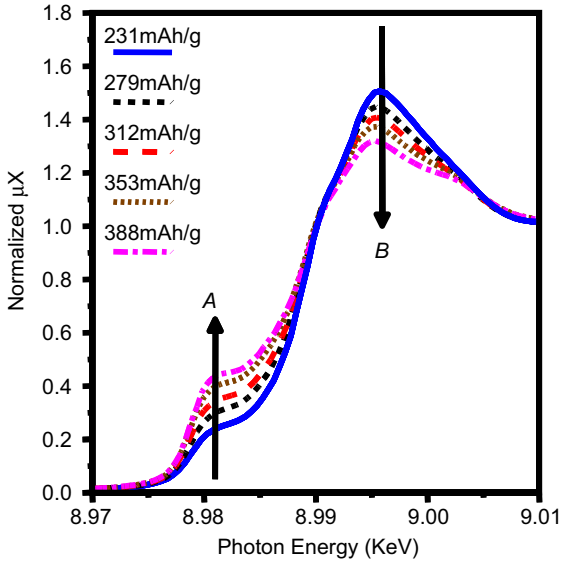

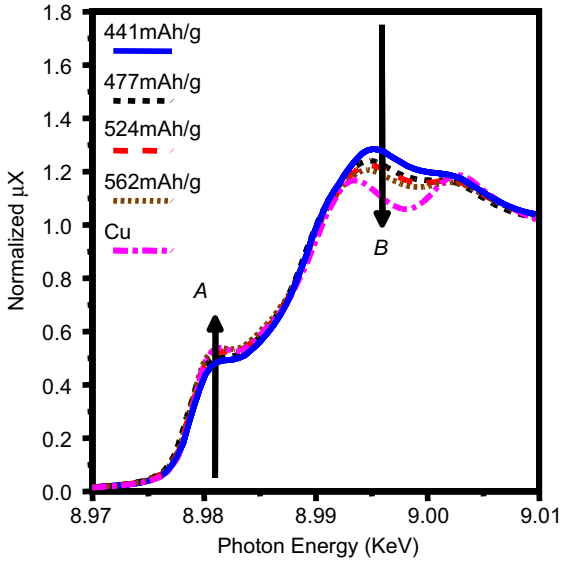

Fig. 4. Cu *K*-edge XANES spectra for the 85 wt% CuF_2–15 wt% MoO_3 nanocomposite cathode collected during the first discharge cycle as a function of state of discharge. The XANES spectrum for a Cu foil is included as reference for metallic Cu.

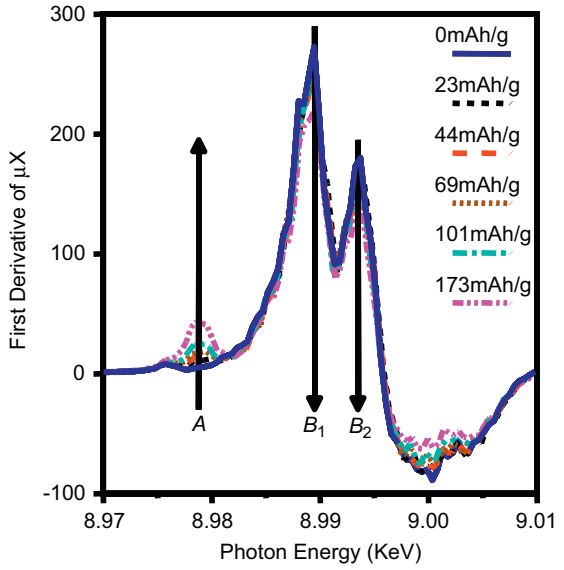

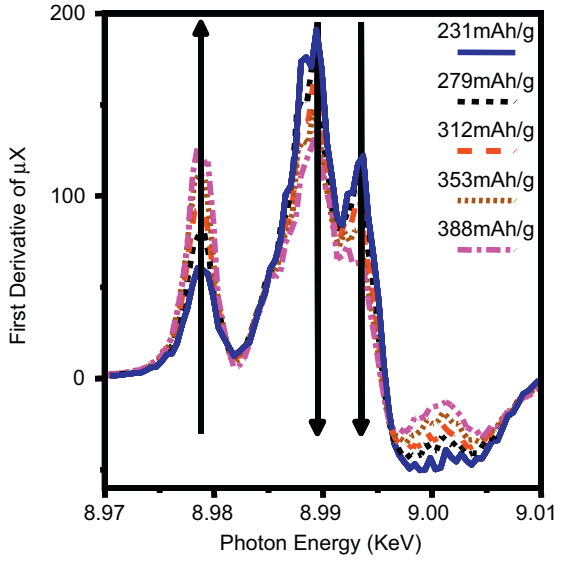

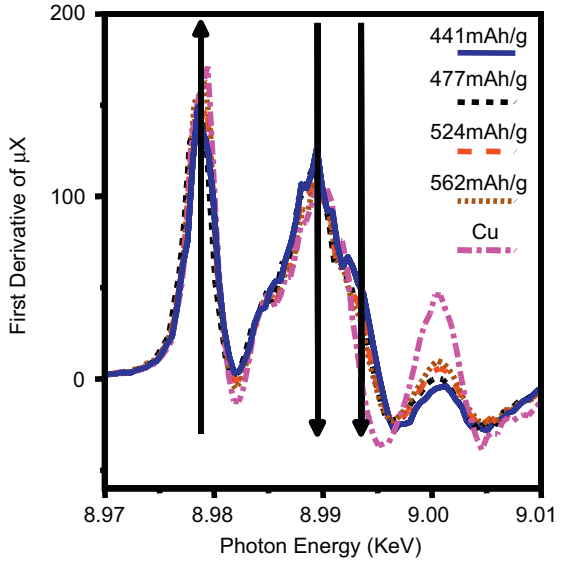

Fig. 5. The first derivative of the Cu *K*-edge XANES spectra for the 85 wt% CuF_2–15 wt% MoO_3 nanocomposite cathode collected during the first discharge cycle as a function of state of discharge. The XANES spectrum for a Cu foil is included as reference for metallic Cu.

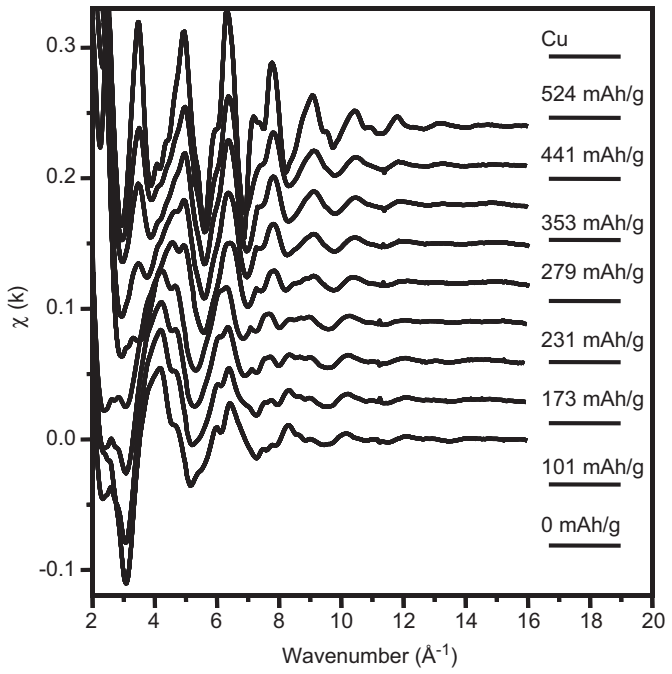

Fig. 6. EXAFS spectra for the 85 wt% CuF_2–15 wt% MoO_3 nanocomposite cathode collected during the first discharge cycle as a function of state of discharge. The spectra are listed from bottom to top with increasing state of discharge. The spectrum of a Cu foil (top spectrum) is included as reference for metallic Cu.

to that of metallic Cu, the amplitudes for the second, third, and fourth shells are still significantly lower than those of metallic Cu. The nonlinear variation in the amplitudes for the fully discharged CuF_2–MoO_3 nanocomposite relative to those of metallic Cu is a clear indication of the highly dispersed nature of the discharged product of the CuF_2–MoO_3 nanocomposite. That is, the discharged product is in the form of Cu nanoparticles embedded in a matrix of lithium fluoride. The effect of particle size on the Fourier transform amplitudes was demonstrated by Bazin et al. [37] for Pt clusters containing 13 and 55 atoms and a Pt foil.

Quantitative analysis of the first shell of Cu nanoparticles and a Cu foil reference are summarized in Table 2. Comparisons of the experimental and simulated Fourier transforms of k^3-weighted Cu *K*-edge EXAFS spectra for the Cu foil and the Cu nanoparticles generated after completely discharging the CuF_2–MoO_3 nanocomposite cathode are shown in Fig. 10. The many body amplitude reduction factors was first determined from the data for the Cu foil by constraining the first shell coordination number to its crystallographic value of 12. Its value was estimated to be 0.98 ± 0.09, which is consistent with that estimated for the CuF_2 nanocomposite (0.85 ± 0.08) within the uncertainty in the data. However, the first shell disorder of 0.0089 Å^2 is somewhat higher than the theoretically estimated values based on force-constant models (0.0077 Å^2 [38]), anharmonic correlated Einstein model (0.0080 Å^2 [39]), and local density approximation model (0.0082 Å^2 [40]). Also, the first shell of Cu foil disorder is somewhat higher than some previously reported experimental values of 0.0077 [41] and 0.0079 Å^2 [42]. The somewhat higher disorder in our case is believed to be due to the high degree of correlation between S_0^2 and the disorder, which is magnified in the case of a single shell fit. Since the many body amplitude reduction factor for the CuF_2 nanocomposite was obtained using multiple shell fits with coordination numbers constrained to their crystallographic values, the degree of correlation between S_0^2 and the disorder in this case is significantly reduced. Hence, we fitted the Cu foil data while constraining S_0^2 to the value for CuF_2 (0.85) and, in this case,

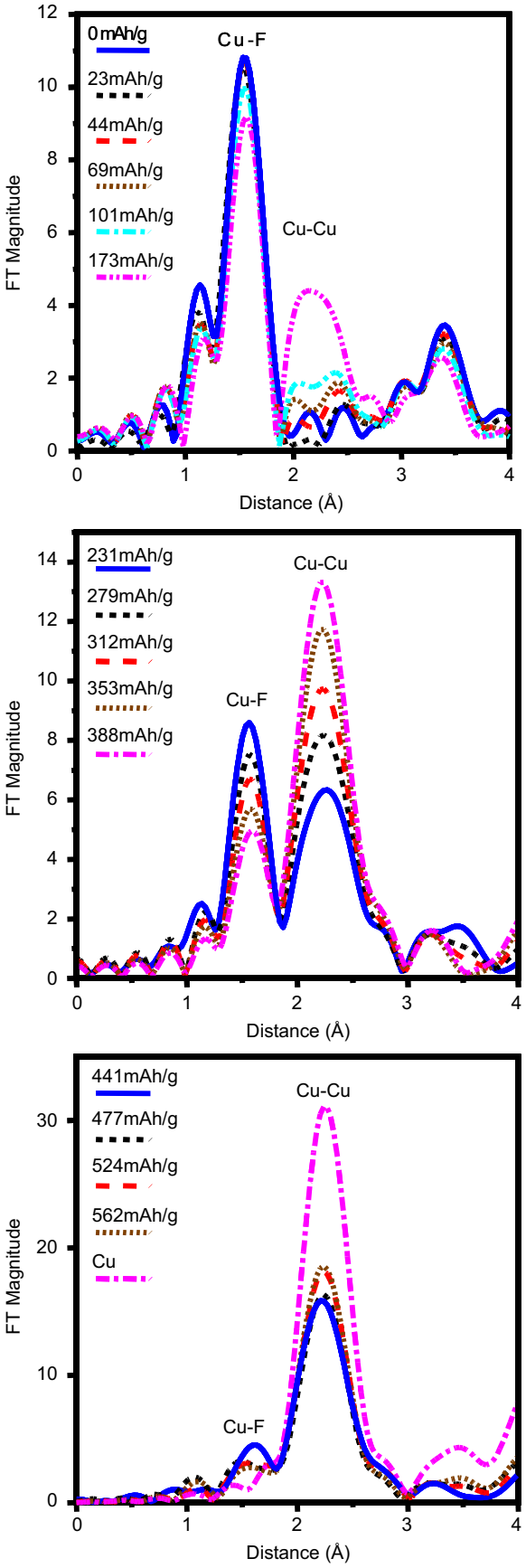

Fig. 7. Evolution of Fourier transforms of k^3-weighted Cu *K*-edge EXAFS spectra for the 85 wt% CuF_2–15 wt% MoO_3 nanocomposite cathode collected during the first discharge cycle as a function of state of discharge. The Fourier transform for a Cu foil is included as reference for metallic Cu. The FT window is 3.0–12.8 Å^{-1}.

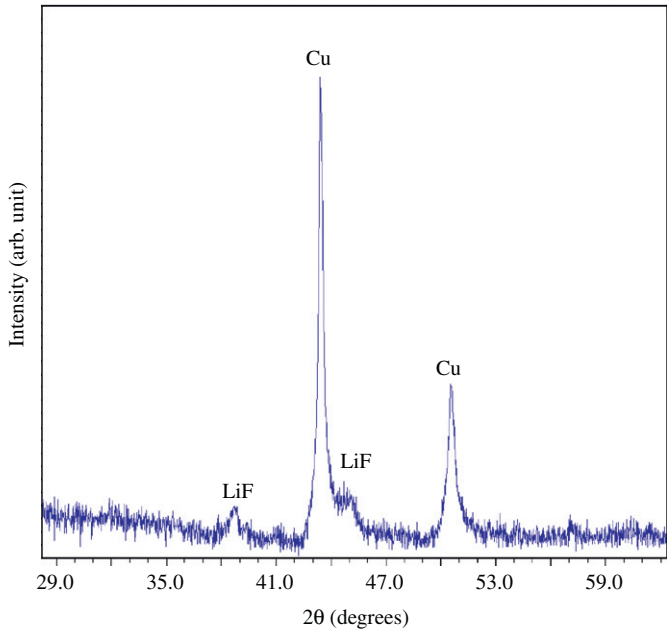

Fig. 8. XRD pattern for a CuF_2–15 wt% MoO_3 nanocomposite cathode discharged to 75% depth of discharge showing formation of LiF and metallic Cu. The data was collected with Cu $K\alpha$ X-rays.

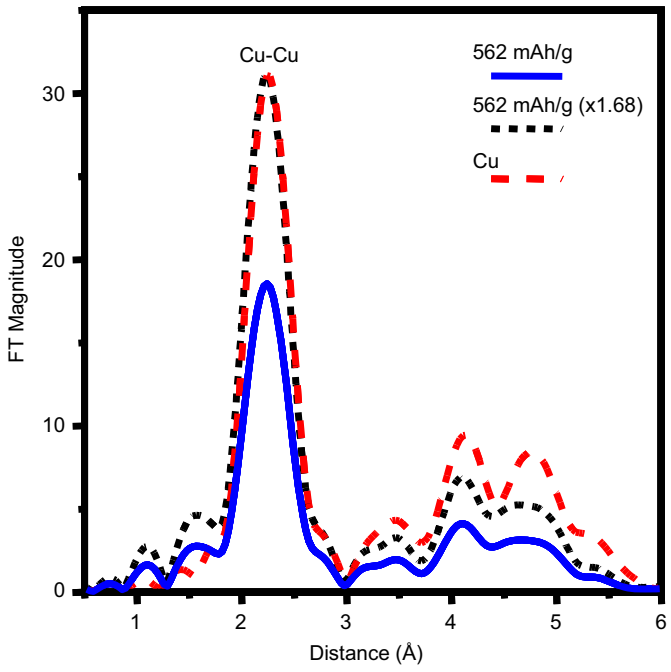

Fig. 9. Comparison of Fourier transforms for the fully discharged 85 wt% CuF_2–15 wt% MoO_3 nanocomposite cathode with that of a Cu foil including contributions from higher coordination spheres. In addition, the Fourier transform for the nanocomposite was scaled so that the first shell amplitude matches that for metallic Cu. The lower amplitudes for the nanocomposite cathode is a clear indication of the highly dispersed nature of the Cu particles formed during the discharge cycle. The FT window is 3.0–12.8 $Å^{-1}$.

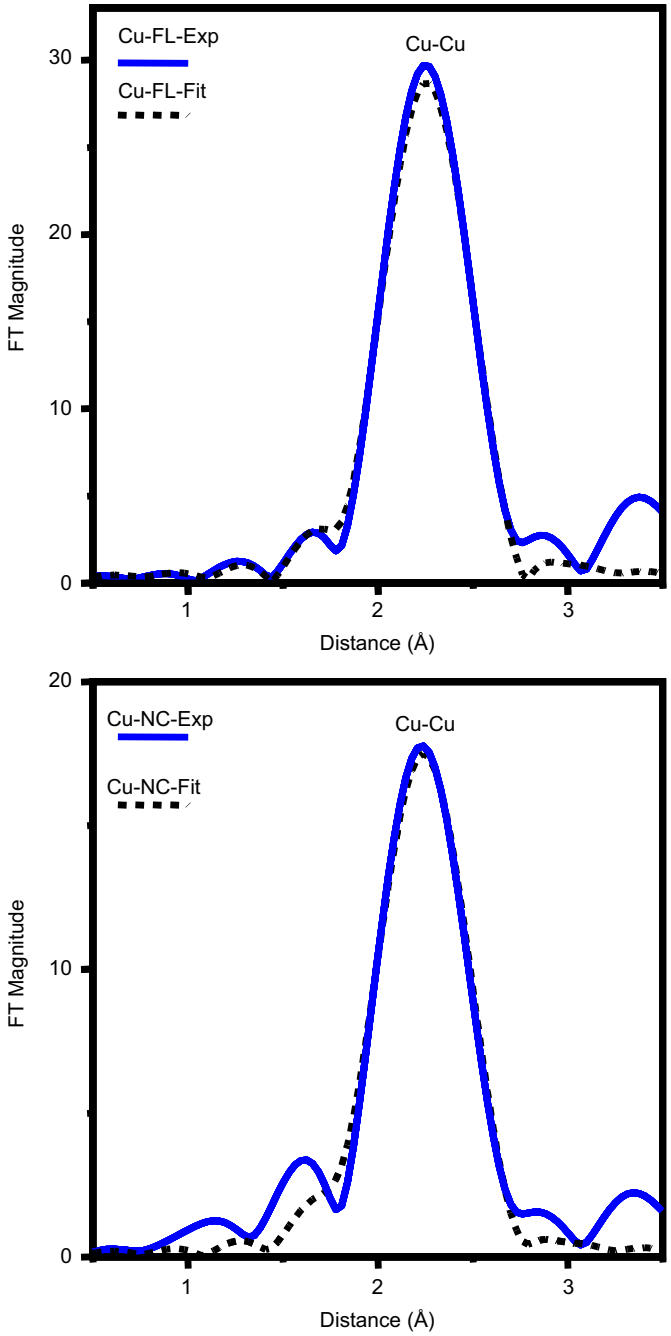

Fig. 10. Comparisons of the experimental and simulated Fourier transforms of k^3-weighted Cu K-edge EXAFS spectra for the Cu foil (top) and the Cu nanoparticles (bottom) after completely discharging the 85 wt% CuF_2–15 wt% MoO_3 nanocomposite cathode. The local structure parameters used for the simulated Fourier transforms are listed in Table 2. The FT window is 3.0–12.8 $Å^{-1}$.

the first shell disorder is 0.0080 $Å^2$, which is in good agreement with the theoretically and experimentally reported values. The value of the many body amplitude reduction factors for CuF_2 was also used in the case of the Cu nanoparticles in order to accurately determine the first shell coordination number and disorder. The first shell distance for the Cu nanoparticles appears to be slightly shorter than that observed for the Cu foil. In addition, the first shell coordination number for the Cu nanoparticles is significantly less than that of the Cu foil due to the highly dispersed nature of the Cu particles. These nanoparticles have a large fraction of their Cu atoms on the surface and, hence, are not fully coordinated. Furthermore, within the uncertainty in the data, the first shell disorder for the Cu nanoparticles is larger than that observed for the Cu foil, which is expected for highly dispersed particles.

As has been demonstrated by many authors [43–46], the coordination number of various coordination spheres can be determined as a function of particle size and morphology using

relatively simple relationships. Assuming the particle shape to be spherical and following the procedure described by Jentys [40], the number of Cu atoms in the cluster is estimated to be in the range 75–1240 atoms with a size in the range 14–32 Å taking into account the uncertainty in the coordination number. Using the relationships between the cluster size and the number of atoms in the cluster with spherical and cubical shapes [38], the particle size is estimated to be in the range 12–30 and 10–24 Å, respectively. Furthermore, based on the relationship between the coordination number and the size of spherical clusters [41], the size of the Cu particles is estimated to be in the range 12–30 Å. All of these estimates give a range 10–32 Å for the diameter of the Cu particles. However, in the case of a bimodal distribution as pointed by Calvin et al. [41], the particle size determined on the basis of the EXAFS coordination number may differ significantly from the true size of the particles. Furthermore, based on a combined investigation of nanoparticles by EXAFS, TEM, and XRD [41], it was noted that EXAFS and XRD determined particle sizes were weighted toward smaller and larger particles, respectively. The Cu particle size of 1–3 nm observed for the fully discharged product of the CuF_2–MoO_3 nanocomposite cathode is significantly smaller than that reported for the fully discharged product of carbon coated nano-CuF_2 cathode [34], which is 9 nm on the basis of the XRD data. The difference is, at least in part, due to the fact that EXAFS determination is weighted toward smaller particles while XRD determination is weighted toward larger particles. This disparity may also be a result of the matrix utilized as the mixed conducting matrix of molybdenum oxyfluoride utilized in the present study may induce the formation of finer Cu nucleation. Finally, we must also consider the effect of the formation of high aspect ratio crystals of nanodimensions and the assumptions brought forth in both sets of calculations.

3.4. Quantitative analysis of Cu content vs. state of discharge

Based on the discharge mechanism and a nominal cell capacity of 528 mAh/g, the percent of Cu in the form of metallic nanoparticles can be estimated from the amount of charge passed assuming that 100% Cu corresponds to a discharge capacity of 528 mAh/g. Any discharge capacity above 528 mAh/g is assumed to be due to side-reactions and/or electrolyte decomposition. In order to examine the conversion efficiency of CuF_2, we also calculated the percent of metallic copper based on the intensity of feature *A* in the XANES spectra. Based on multiple scattering calculations, Greaves et al. [47] have shown that the intensity of feature *A* for metallic Cu (i.e., Cu foil) can be produced by only including the first shell of Cu atoms (i.e., a cluster with radius of 2.56 Å, which contains 13 atoms). The intensity of this feature remained relatively unchanged when the multiple scattering calculations included the second, third and fourth shells of Cu atoms (i.e., a cluster with radius of 5.09 Å, which contains 55 atoms). The expansion of the cluster radius from 2.56 to 5.09 Å, however, was essential to correctly produce other metallic Cu XANES features present at higher energies relative to the energy of feature *A*. In the case of the Cu foil, all atoms are equivalent and the experimentally measured intensity of feature *A* represents the intrinsic intensity for metallic Cu. In the case of nano-clusters, one would need to average over all atoms in the cluster since surface atoms are not fully coordinated. The effect of cluster size on the intensity of the Cu XANES features was investigated by Bazin et al. [35] using Cu clusters containing 13 and 55 atoms. The intensity of feature *A* for the 13-atom Cu cluster was found to be slightly larger than that for the 55-atoms Cu cluster. The small variation in the intensity of feature *A* with cluster size is due to the fact that this feature can be produced by including XAFS contributions from only the first shell of atoms without the need to include contributions from higher coordination spheres. The size effect on the intensity of the white line for spherical Pt clusters containing 13, 19, and 43 atoms was found to be very small [48]. In this study, the XANES features which follow the Pt L_3-edge white line were found to be more sensitive to the size of the spherical Pt clusters. However, more variations in the XANES region were found for non-spherical clusters containing 3–9 Pt atoms. The intensity of the white line for these small clusters was found to be comparable to or greater than that of bulk Pt depending on the assumed size and the shape of the clusters.

Based on the above discussions, we believe that it is possible to use the variations in the intensity of feature *A* in the XANES spectra of the discharged CuF_2–MoO_3 nanocomposite to determine the approximate percent of metallic Cu as a function of state discharge. The percent of Cu was estimated assuming that the intensity of feature *A* for the discharged nanocomposite cathode is a linear combination of contributions from metallic Cu and CuF_2 in the discharged nanocomposite cathode. That is, using the formula

$$Y = f^{*}I_{Cu} + (1-f)^{*}I_{CuF2}$$

where Y is the intensity of feature *A* for the nanocomposite cathode as a function of state of discharge, f is the fraction of metallic Cu, $(1-f)$ is the fraction of Cu in the form of CuF_2, I_{Cu} is the experimentally measured intensity of feature *A* for a Cu foil which is equal to 0.5448 and I_{CuF2} is the experimentally measured absorption for CuF_2 at the energy of feature *A* for the Cu foil which is equal to 0.0659. On this basis, the percents of Cu in the form of nanoparticles are listed in Table 3 as a function of state of discharge. The ratios of Cu estimated from depth of discharge to Cu estimated from XANES spectra are also listed in Table 3. In general, we find good agreement between the Cu content based on depth of discharge and that based on the intensity of feature *A* in the XANES spectra, except during the initial stages of discharge.

As one discharges the cathode, the XANES spectra (Fig. 4) and Fourier transforms data (Fig. 6) displayed only small changes upon 69 mAh/g of discharge capacity. However, significant changes in the XANES spectra and Fourier transforms data evolved after more than 69 mAh/g of discharge capacity as indicated by the spectrum which corresponds to a discharge capacity of 101 mAh/g. Clearly, during the initial stages of discharge, at least some of the lithium was not interacting directly with CuF_2. The lack of significant changes during the initial stages of discharge may be attributed to one of the following scenarios. First, some of the initial lithium may be used up during the formation of a SEI film, by pseudocapacitive side reactions involving surface contamination, or simply and most likely an insertion reaction within the molybdenum oxyfluoride matrix that is formed in situ. Second, the initial stages of discharge may proceed via the intercalation of Li into CuF_2 leading to the formation of $LiCuF_2$ on the defect surface of the 20 nm CuF_2 domains. If this to occur, a fraction of the Cu^{2+} will be reduced to Cu^{1+} for charge neutrality. However, the formation of Cu^{1+} cannot be confirmed based on examination of the derivative of XANES spectra (Fig. 5). Hence, the formation of $LiCuF_2$ is ruled out based on the XANES data. Furthermore, the formation of Cu^{1+} was not observed during the initial stages of discharge of a carbon coated nano-CuF_2 cathode as reported by Yamakawa et al. [34].

3.5. Summary and conclusions

The conversion reaction of the CuF_2–MoO_3 nanocomposite during the lithiation process was investigated by X-ray absorption spectroscopy under in situ conditions. Both the XANES and Fourier transforms of EXAFS spectra demonstrate the formation of metallic Cu during the discharge cycle; this is consistent with

Table 3
Summary of the intensity of feature *A* in the XANES spectra of the 85 wt% CuF_2–15 wt% MoO_3 nanocomposite cathode as a function of state of discharge, and percents of Cu in metallic form as determined from depth of discharge (DOD) and the XANES spectra.

State of discharge (mAh/g of CuF_2)	Intensity[a]	% Cu (DOD)[b]	% Cu (XANES)[c]	Ratio Cu^c/Cu^b
0	0.0659	0.0	0.0	N/A
22.6	0.0812	4.3	3.2	0.75
43.7	0.0907	8.3	5.2	0.63
68.7	0.1040	13.0	8.0	0.61
101.4	0.1236	19.2	12.0	0.63
132.1	0.1470	25.0	16.9	0.68
147.9	0.1620	28.0	20.1	0.72
172.9	0.1829	32.7	24.4	0.75
231.0	0.2466	43.7	37.7	0.86
246.4	0.2663	46.6	41.8	0.90
266.6	0.2927	50.5	47.4	0.94
278.6	0.3075	52.7	50.4	0.96
289.2	0.3205	54.7	53.2	0.97
305.0	0.3432	57.7	57.9	1.00
311.7	0.3520	59.0	59.7	1.01
332.4	0.3826	62.9	66.1	1.05
353.1	0.4068	66.8	71.2	1.07
367.4	0.4421	69.5	78.6	1.13
387.6	0.4441	73.4	79.0	1.08
416.0	0.4676	78.7	83.9	1.07
441.0	0.4879	83.5	88.1	1.06
457.3	0.4923	86.5	89.0	1.03
477.4	0.5032	90.4	91.3	1.01
524.1	0.5231	99.2	95.5	0.96
546.2	0.5440	100.0	99.8	1.00
561.6	0.5447	100.0	100.0	1.00
Cu foil	0.5448			

[a] Intensity of feature *A* as measured directly from the XANES spectra.
[b] % of metallic Cu based on depth of discharge assuming that it varied linearly between 0 mAh/g (100% CuF_2) and the nominal capacity of 528 mAh/g (100% Cu). Any discharge capacity above 528.0 mAh/g of CuF_2 was assumed to be due to side reactions and/or electrolyte decomposition and was ignored for the purpose of these calculations.
[c] % of metallic Cu based on the intensity of feature *A* in the Cu *K*-edge XANES spectra.

the electrochemical conversion of CuF_2 into Cu and LiF. The evolution of the XANES and Fourier transforms of EXAFS spectra during the discharge cycle displayed a good correlation with the state of discharge of the nanocomposite cathode. We show that Cu is present in a highly dispersed in the fully discharged state of the electrode. Quantitative analysis of the first shell of Cu in the Fourier transform for the fully discharged nanocomposite revealed the formation of Cu clusters with an average size in the range 1–3 nm. These results suggest that the Cu does not aggregate into large domains, but does not preclude the possibility of larger nanothin aggregates of high aspect ratios. The average size of the discharge product for the nanocomposite is significantly smaller than the 9 nm size reported by Yamakawa et al. [34] on the basis of the XRD data for the discharged product of carbon coated nano-CuF_2 cathode. It is to be noted that the difference between the particle size for the nanocomposite and the carbon coated nano-CuF_2 could be at least in part due to the fact that EXAFS determined particle size is weighted toward smaller particles while that determined by XRD is weighted toward larger particles.

The characterization of the nucleation and growth process is a critical component to the understanding and improvement of conversion and reversible conversion processes in battery electrodes. The distribution of the converted metal and salts play a key role in the kinetics, and kinetic pathways of reaction along with stability and cycling. Such characterization is not always easy especially in the early stages of the reaction. The applied XANES and EXAFS based approaches to coordination shell growth can complement other characterization including X-ray diffraction, pair distribution function analysis and high resolution microscopy in bringing forth a complete picture of the morphological evolution of such reactions.

Acknowledgments

ANM acknowledges support by the Carderock Division of the Naval Surface Warfare Center's In-house Laboratory Independent Research Program administrated under ONR's Program Element 0601152N. GGA acknowledges support by the U.S. Government. The XAS experiments were conducted at the National Synchrotron Light Source of Brookhaven National Laboratory, which is supported by the US Department of Energy, Office of Basic Energy Sciences, under Contract no. DE-AC02-98CH10886. This work at Kookmin University was supported by Priority Research Centers Program (2009-0093814) and the CMPS (R11-2005-048-00000-0) of MEST/NRF.

References

[1] H. Li, G. Richter, J. Maier, Adv. Mater. 15 (2003) 736–739.
[2] F. Badway, N. Pereira, F. Cosandey, G.G. Amatucci, J. Electrochem. Soc. 150 (2003) A1209–A1218.
[3] F. Plitz, J. Badway, A. Al-Sharab, F. DuPasquier, G.G. Cosandey, Amatucci, J. Electrochem. Soc. 152 (2005) A307–A315.
[4] M. Bervas, F. Badway, L.C. Klein, G.G. Amatucci, Electrochem. Solid-State Lett. 8 (2005) A179–A183.
[5] H. Li, P. Balaya, J. Maier, J. Electrochem. Soc. 151 (2004) A1878–A1885.
[6] M. Bervas, L.C. Klein, G.G. Amatucci, J. Electrochem. Soc. 153 (2006) A159–A170.
[7] M. Bervas, A.N. Mansour, W.S. Yoon, J. Al-Sharab, F. Badway, F. Cosandey, L.C. Klein, G.G. Amatucci, J. Electrochem. Soc. 153 (2006) A799–A808.
[8] F. Badway, A. Mansour, I. Plitz, N. Pereira, L. Weinstein, W. Yourey, G.G. Amatucci, Mater. Res. Soc. Symp. Proc. 972 (2007) 0972-AA07-01-BB08-1.
[9] G.G. Amatucci, N. Pereira, J. Fluorine Chem. 128 (2007) 243–262.
[10] H.F. Bauman,Development of lithium–cupric fluoride batteries, in: Proceedings of the 20th Annual Power Sources Conference, PSC Publications, May 1966, pp 73–76.

[11] H.F. Bauman, Development of the copper fluoride–lithium couple for limited-cycle secondary battery, in: Proceedings of the 18th Annual Power Sources Conference, PSC Publications, May 1964, pp. 89–91.
[12] W.E. Elliott, J.R. Huff, G.L. Simmons, G.D. McDonald, J.L. Jamrozy, W.L. Towle, A program to develop a high-energy density primary battery with a minimum of 200 W hours per pound of total battery weight, Contract report NASA CR-54873 December 31, 1965.
[13] S.G. Abens, T.X. Mahy, W.C. Merz, Development of high energy density primary batteries, Contract report NASA CR-54859, December 28, 1965.
[14] J. Farrar, R. Keller, C.J. Mazac, in: Proceedings of the 18th Annual Power Sources Conference, May 1964, PSC Publications, pp. 92–94.
[15] F. Badway, A.N. Mansour, N. Pereira, J.F. Al-Sharab, F. Cosandey, I. Plitz, G.G. Amatucci, Chem. Mater. 19 (2007) 4129–4141.
[16] M. Balasubramanian, X. Sun, X.Q. Yang, J. McBreen, J. Power Sources 92 (2001) 1–8.
[17] D.E. Sayers, S.M. Heald, M.A. Pick, J.I. Budnick, E.A. Stern, J. Wong, Nucl. Instrum. Methods Phys. Res. 208 (1983) 631–635.
[18] M.O. Krause, J.H. Oliver, J. Phys. Chem. Ref. Data 8 (1979) 329–338.
[19] K.Q. Lu, E.A. Stern, Nucl. Instrum. Methods 212 (1983) 475–478.
[20] E.A. Stern, K. Kim, Phys. Rev. B 23 (1981) 3781–3787.
[21] D.E. Sayers, B.A. Bunker, in: D.C. Koningsberger, R. Prins (Eds.), X-ray Absorption: Principles, Applications, Techniques of EXAFS, SEXAFS and XANES, Wiley, New York, 1988 Chapter 6.
[22] J.W. Cook Jr., D.E. Sayers, J. Appl. Phys. 52 (1981) 5024–5031.
[23] T. Ressler, J. Synchrotron Radiat. 5 (2000) 118–122.
[24] T. Ressler, J. Phys. IV 7 (1997) C2-269-C2-270.
[25] E.A. Stern, M. Newville, B. Ravel, Y. Yacoby, D. Haskel, Physica B 208–209 (1995) 117–120.
[26] A.L. Ankuudinov, B. Ravel, J.J. Rehr, S.D. Conradson, Phys. Rev. B. 58 (1998) 7565–7576.
[27] A.L. Ankudinov, C.E. Boulden, J.J. Rehr, J. Sims, H. Hung, Phys. Rev. B 65 (2002) 104107-1-104107-11.
[28] P. Villars, L.D. Calvert, Pearson's Handbook of Crystallographic Data for Intermetallic Phases, vol. 3, American Society for Metals, Metals Park, OH, 1985, p. 1023.
[29] P. Fischer, W. Halg, D. Schwarzenbach, H. Gamsjager, J. Phys. Chem. Solids 35 (1974) 1683–1689.
[30] P.C. Burns, Frank C. Hawthorne, Powder Diffraction 6 (3) (1991) 156–158.
[31] E.A. Stern, Phys. Rev. B 48 (1993) 9825–9827.
[32] J.M. Tranquada, S.M. Heald, A.R. Moodenbaugh, Phys. Rev. B 36 (1987) 5263–5274.
[33] J.-H. Choy, J.-B. Yoon, H. Jung, J. Phys. Chem. B 106 (2002) 11120–11126.
[34] N. Yamakawa, M. Jiang, C.P. Grey, Chem. Mater. 21 (2009) 3162–3176.
[35] M. Giorgetti, S. Mukerjee, S. Passerini, J. McBreen, W.H. Smyrl, J. Electrochem. Soc. 148 (2001) A768–A774.
[36] P. Conti, S. Zamponi, M. Giorgetti, M. Berrettoni, W.H. Smyrl, Anal. Chem. 82 (2010) 3629–3635.
[37] D.C. Bazin, D.A. Sayers, J.J. Rehr, J. Phys. Chem. B 101 (1997) 11040–11050.
[38] E. Sevillano, H. Meuth, J.J. Rehr, Phys. Rev. B 20 (1979) 4908–4911.
[39] N.V. Hung, J.J. Rehr, Phys. Rev. B 56 (1997) 43–46.
[40] F.D. Vila, J.J. Rehr, H.H. Rossner, H.J. Krappe, Phys. Rev. B 76 (2007) 014301-1-014301-11.
[41] R.B. Greegor, F.W. Lytle, Phys. Rev. B. 20 (1979) 4902–4907.
[42] E.A. Stern, B.A. Bunker, S.M. Heald, Phys. Rev. B. (1980) 5521–5539.
[43] R.B. Greegor, F.W. Lytle, J. Catal. 63 (1980) 476–486.
[44] J.M. Montejano-Carrizale, F. Aguilera-Granja, J.L. Moran-Lopez, Nanostruct. Mater. 8 (1997) 269–287.
[45] A. Jentys, Phys. Chem. Phys. 1 (1999) 4059–4063.
[46] S. Calvin, N.M. Miller, R. Goswami, S.F. Cheng, S.P. Mulvaney, L.J. Whitman, V.G. Harris, J. Appl. Phys. 94 (2003) 778–783.
[47] G.N. Greaves, P.J. Durham, G. Diakun, P. Quinn, Nature 294 (1981) 139–142.
[48] A.L. Ankudinov, J.J. Rehr, J.J. Low, S.R. Bare, J. Chem. Phys. 116 (2002) 1911–1919.